# SHSLBM Simulation of Hybrid Nanofluid Thermal Convection at High Rayleigh Numbers

Yuan Ma[a,b,*] and Zhigang Yang[a,b,c,*]

[a] Shanghai Automotive Wind Tunnel Center, Tongji University, No.4800, Cao'an Road, Shanghai, China, 201804
[b] Shanghai Key Lab of Vehicle Aerodynamics and Vehicle Thermal Management Systems, No.4800, Cao'an Road, Shanghai, China, 201804
[c] Beijing Aeronautical Science & Technology Research Institute, Beijing, China, 102211

*Corresponding author. E-mail address: 1510812@tongji.edu.cn (Yuan Ma), zhigang.yang@sawtc.com (Zhigang Yang)

## ABSTRACT

A new method called simplified and highly stable lattice Boltzmann method (SHSLBM) was used to simulate the hybrid nanofluid natural convection and heat transfer in a square enclosure with a heating obstacle at high Rayleigh numbers. There are four fins on the heating obstacle to affect the flow pattern and heat transfer performance. SHSLBM is based on the lattice Boltzmann framework. The effects of Rayleigh number ($10^6 \leq Ra \leq 10^9$), nanoparticle volume fraction ($0 \leq \phi \leq 0.05$) and length of fin ($0.1 \leq h \leq 0.3$) on the flow pattern, temperature distribution and heat transfer characteristics were illustrated and analyzed. The benchmark simulation results were performed to the method of validation. Three kinds of flow patterns (steady symmetry, unsteady symmetry and unsteady asymmetry) can be observed at various Rayleigh number. At $\phi = 0.01$, when the $Ra$ increases from $1\times10^6$ to $1\times10^9$, the transitions of flow regime from steady symmetry state to unsteady asymmetry state occur. The $\phi$ and $h$ also affects the flow pattern significantly. At higher $\phi$, the flow inside the enclosure is steadier and the effect of $h$ on the flow pattern varies at different $Ra$.

*Keywords*: SHSLBM; High *Ra*; Nanofluid; Fin; Natural convection; Heat transfer

## 1. Introduction

Thermal convection in an enclosure has been a significant subject of numerical simulations in the past several decades.[1,2,3] The flow pattern and heat transfer characteristics have comprehensive application in the engineering applications such as electronic equipment systems, heat exchangers, solar energy systems and chemical reaction systems.[4] Bhardwaj et al.[5] analyzed the natural convection and heat transfer in a porous two-dimensional right-angled triangular cavity with undulatoy walls. It has been observed that the maximum Nusselt number of the left wall increases 53% at $Ra = 10^6$ comparing with the no-undulation case. Esfe et al.[6] numerically investigated the natural convection in a trapezoidal cavity. They found that the average Nusselt number ($Nu$) increases by decreasing the inclination angle ($\gamma$) at low Rayleigh numbers ($Ra \leq 10^4$). However, at $Ra = 10^6$, the average Nu increases firstly and then decreases and obtains the maximum value at $\gamma = 30$.

Ma et al.[7] studied the effects of nanofluid and aspect ratio (AR) on the flow pattern and heat transfer characteristics in a baffled U-shaped enclosure in the presence of a magnetic field. It can be obtained that the change of $AR$ cannot affect the flow pattern and the average $Nu$ increases by increasing $AR$. Haghighi et al.[8] experimentally studied the natural convection in plate-fin based heat sinks. Six different types of fins are conducted in their study. They found that the thermal resistance increases as decreasing the gap between the fins. Besides, the plate cubic pin-fin heat sinks have a better heat transfer performance.

Recently, nanofluid has been studied to enhance the rate of heat transfer due to its high heat transfer performance.[9,10] Ma et al.[11] numerically studied the Ag-MgO/water hybrid nanofluid convection and heat transfer in a channel with active heaters and coolers in the presence of magnetic field. They found that the average Nusselt number is increasing function of nanoparticle volume fraction and Reynolds number, but a decreasing function of Hartmann number. Hatami and Safari[12] performed a numerical simulation to investigate the nanofluid natural convection and heat transfer in an enclosure with wavy walls and an inside heating cylinder. The results showed that the heat transfer performance is best when the obstacle is located on the center for all the

volume fraction of nanoparticles.

Lattice Boltzmann method has been widely used to simulate the problem of fluid flow and heat transfer due to its advantages such as easy to implement, natural parallel and easy to deal with the complex boundaries. Recently, many new methods based on the LBM have been developed. Chikatamarla and Karlin[13] proposed a new model named entropic lattice Boltzmann method (ELBM) to simulate the multiphase flows. They found that the ELBM is suitable for the high Reynolds number and high Weber numbers for two-phase flows. A high-order simplified thermal lattice Boltzmann method (HSTLBM) is developed by Chen et al.[14] to study the incompressible thermal flows accurately and efficiently. After the validation of benchmark simulations, HSTLBM is treated as an efficient method to solve the thermal convection at high Rayleigh numbers. Jami et al.[15] developed a new thermal MRT-LBM for simulating the convection. They examined the different convection cases when the Rayleigh number is less than $10^8$. After the comparison and validation, the method is proved to solve the similar problems. Chen et al.[16] developed a new method named simplified and highly stable lattice Boltzmann method (SHSLBM) to solve the fluid flow problems. The method showed a very nice stability characteristic in high Reynolds number.

The literature shows that the nanofluid flow and heat transfer at high Rayleigh numbers did not get enough attention. Thus, the first objective of the present work is to study the flow pattern and heat transfer characteristics of nanofluid natural convection at high Rayleigh numbers. Four fins are mounted on the heating obstacle in the storage unit to enhance the heat transfer rate and the effects of fins on the flow regime and heat transfer are investigated, which is the second objective of the work. Moreover, in the present work, the SHSLBM is developed into the thermal filed and used to solve the governing equations of the present simulations. The effects of Rayleigh number ($10^6 \leq Ra \leq 10^9$), nanoparticle volume fraction ($0 \leq \phi \leq 0.05$) and length of fin ($0.1 \leq h \leq 0.3$) on the flow pattern, temperature distribution and Nusselt number are investigated.

## 2. Mathematical formulation

*2.1. Problem definition*

The Ag-$TiO_2$/water hybrid nanofluid flow and heat transfer in a thermal energy storage with four fins are considered in Fig. 1. Table 1 illustrates the thermophysical properties of pure water and nanoparticles. In this finned heat storage unit, the four fins are mounted on the four walls of the square obstacle and their temperature is fixed at $T_h = 1$. The four walls of the heat storage unit have a constant temperature ($T_c$) which is lower than $T_h$. $P_1$ and $P_2$ are two monitoring points inside the finned heat storage unit.

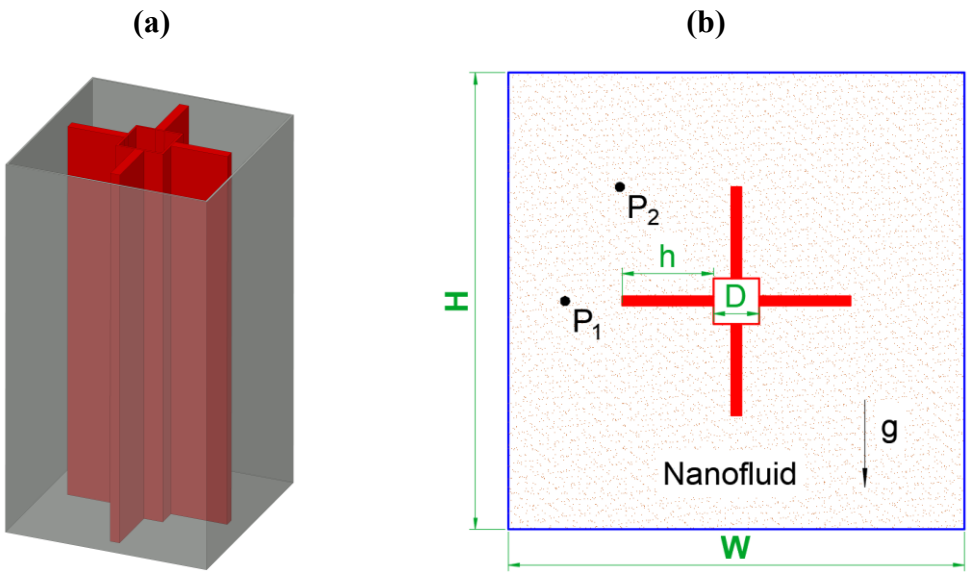


Fig. 1 3D and 2D schematic diagram under consideration in the present work.

Table 1. Thermophysical properties of pure water and nanoparticles at 25° C.

| Property | Pure water | Ag (nanoparticles) | $TiO_2$ (nanoparticles) |
|---|---|---|---|
| $C_p$ (J/kg K) | 4179 | 235 | 686.2 |
| $\rho$ (kg/m$^3$) | 997.1 | 10500 | 4250 |
| $K$ (W/m k) | 0.623 | 429 | 8.9538 |
| $\beta\times10^5$ (K$^{-1}$) | 21 | 1.89 | 0.9 |
| $\mu\times 10^4$ (kg/m s) | 8.55 | - | - |

*2.2. Standard LBM*

The standard thermal LBM of $D_2Q_9$ model[17] is firstly introduced in this section.

For the flow field:

$$f_i(x + e_i\delta_t, t + \delta_t) = f_i(x,t) + \frac{\delta_t}{\tau_v}[f_i^{eq}(x,t) - f_i(x,t)] + \Delta t \boldsymbol{e}_i F_i \quad (1)$$

For the thermal field:

$$g_i(x + e_i\delta_t, t + \delta_t) = g_i(x,t) + \frac{\Delta t}{\tau_c}[g_i^{eq}(x,t) - g_i(x,t)] \quad (2)$$

$f_i^{eq}$ and $g_i^{eq}$ denotes the equilibrium distribution function.

$$f_i^{eq} = w_i\rho[1 + \frac{\boldsymbol{e_i u}}{c_s^2} + \frac{1}{2}\frac{(\boldsymbol{e_i u})^2}{c_s^4} - \frac{1}{2}\frac{\boldsymbol{u}^2}{c_s^2}] \quad (3)$$

$$g_i^{eq} = w_i T[1 + \frac{\boldsymbol{e_i u}}{c_s^2}] \quad (4)$$

where $\rho$ is the lattice fluid density, $T$ is the lattice fluid temperature and the weight function $w_i$ has the value of $w_0 = 4/9,\ w_{1-4} = 1/9,\ w_{5-8} = 1/36$. The force term in Eq. (1) is:

$$F_i = 3w_i\rho g_y \beta(T - T_m) \quad (5)$$

where $\rho$, $g_y$, $\beta$ , $T$, $T_m$ stand for local density, gravitational acceleration vector, thermal expansion coefficient, local temperature and the average temperature $T_m = (T_h + T_c)/2$, respectively.

$v$ and $\alpha$ are kinetic viscosity and thermal diffusivity, respectively. The relaxation time for the flow and temperature fields, $\tau_v$ and $\tau_c$, can be defined as

$$\tau_v = 0.5 + v\frac{1}{\delta t c_s^2} \quad (6)$$

$$\tau_c = 0.5 + \alpha\frac{1}{\delta t c_s^2} \quad (7)$$

where $c_s = c/\sqrt{3}$ is the speed of sound.

The macroscopic variables (density, momentum and temperature) can be calculated with the following formula:

$$\rho = \sum_i f_i,\ \rho\boldsymbol{u} = \sum_i e_i f_i,\ T = \sum_i g_i \quad (8)$$

*2.2. SHSLBM*

Based on the thermal LBM above, thermal SHSLBM was reported and used in the current research. Formulations of thermal SHSLBM includes two steps, which are as follows:

Predictor step:

$$\rho^* = \sum_i f_\alpha^{eq}\,(\boldsymbol{r} - \boldsymbol{e}_i\delta_t, t - \delta_t) \tag{9}$$

$$\rho^*\boldsymbol{u}^* = \sum_\alpha \boldsymbol{e}_i\, f_i^{eq}(\boldsymbol{r} - \boldsymbol{e}_i\delta_t, t - \delta_t) \tag{10}$$

$$\rho^* e^* = \sum_i g_i^{eq}(\boldsymbol{r} - \boldsymbol{e}_i\delta_t, t - \delta_t) \tag{11}$$

Corrector step:

$$\rho(\boldsymbol{r}, t) = \rho^* \tag{12}$$

$$\rho(\boldsymbol{r}, t)\boldsymbol{u}(\boldsymbol{r}, t) = \rho^*\boldsymbol{u}^* + (\tau_v - 1)\sum_i \boldsymbol{e}_i\, f_\alpha^{eq}(\boldsymbol{r} + \boldsymbol{e}_i\delta_t, t) - (\tau_v - 1)\rho(\boldsymbol{r}, t - \delta_t)\boldsymbol{u}(\boldsymbol{r}, t - \delta_t) + F_E\delta_t \tag{13}$$

$$\rho(\boldsymbol{r}, t)e(\boldsymbol{r}, t) = \rho^* e^* + (\tau_c - 1)\sum_i g_i^{eq}(\boldsymbol{r} + \boldsymbol{e}_i\delta_t, t) - (\tau_c - 1)\rho(\boldsymbol{r}, t - \delta_t)e(\boldsymbol{r}, t - \delta_t) \tag{14}$$

$$F_E = \rho g_y \beta(T - T_m) \tag{15}$$

*2.4. Nanofluid thermo-physical properties*

The density, specific heat capacity at constant pressure and thermal expansion coefficient of the hybrid nanofluid are calculated as follows:

$$\rho_{nf} = \phi_1\rho_{s_1} + \phi_2\rho_{s_2} + (1 - \phi)\rho_f \tag{16}$$

$$(\rho c_p)_{nf} = \phi_1(\rho c_p)_{s_1} + \phi_2(\rho c_p)_{s_2} + (1 - \phi)(\rho c_p)_f \tag{17}$$

$$(\rho\beta)_{nf} = \phi_1(\rho\beta)_{s_1} + \phi_2(\rho\beta)_{s_2} + (1 - \phi)(\rho\beta)_f \tag{18}$$

where $\phi_1$, $\phi_2$, $\rho_{s1}$, $\rho_{s2}$, $(c_p)_{s1}$, $(c_p)_{s2}$, $(\beta)_{s1}$, $(\beta)_{s2}$ are the volume fraction, density, specific heat capacity at constant pressure and thermal expansion coefficient of the two different nanoparticles, respectively. Also, $\phi$ is the overall volume fraction of two types of nanoparticles in hybrid nanofluid and is determined by

$$\phi = \phi_1 + \phi_2 \tag{19}$$

The effective thermal conductivity and effective viscosity of nanofluid are obtained by:

$$k_{nf} = \frac{(k_{hs}+2k_f)-2\phi(k_f-k_{hs})}{(k_{hs}+2k_f)+\phi(k_f-k_{hs})}k_f \tag{20}$$

with

$$k_{hs} = \frac{\phi_1 k_{s_1}+\phi_2 k_{s_2}}{\phi} \tag{21}$$

The viscosity of nanofluid can be calculated as:

$$\mu_{nf} = \frac{\mu_f}{(1-\phi)^{2.5}} \tag{22}$$

The nanofluid thermal diffusivity and Prandtl number are determined as

$$\alpha_{nf} = \frac{k_{nf}}{(\rho c_p)_{nf}} \tag{23}$$

$$\mathrm{Pr}_{nf} = \frac{(\mu c_p)_{nf}}{k_{nf}} \tag{24}$$

The local Nusselt number of the horizontal boundary can be calculated by

$$Nu_{loc} = -(\frac{k_{nf}}{k_f})(\frac{\partial T}{\partial y}) \tag{25}$$

Finally, the average Nusselt number can be calculated by the integrating of the local Nusselt number along the heater and the cooler.

## 3. Verification of the simulation

In this section, the SHSLBM results are verified by well-know cases in the literature. Fig. 2 shows the streamlines and isotherms inside a square enclosure at different Rayleigh numbers. The temperature of the left wall of the enclosure is fixed as $T_h = 1$ and the right wall is set as a low temperature $T_c = 0$. The top and bottom walls of the enclosure are adiabatic. It can be seen that the obtained results from the present code are in good agreement with those in the previous papers[18,19].

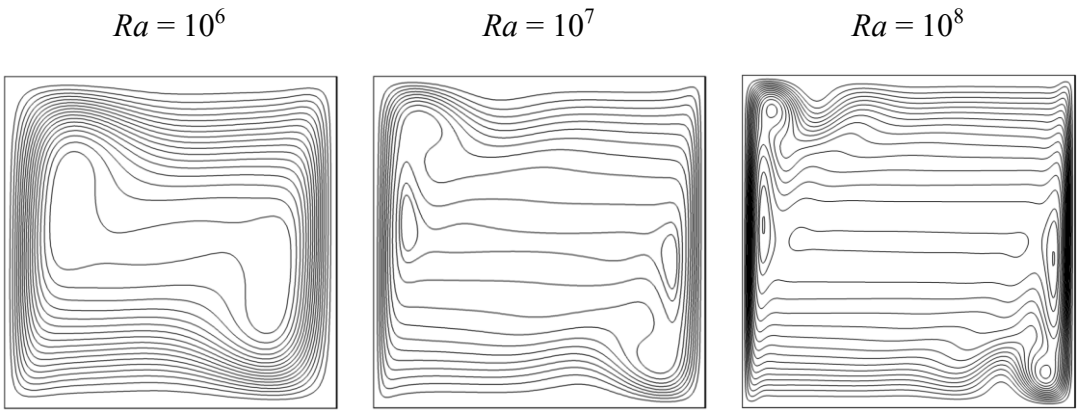

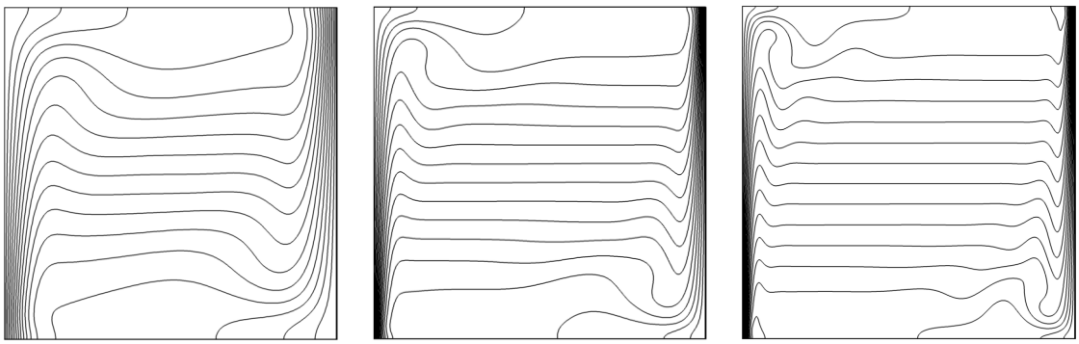

Fig. 2 The streamlines (top) and isotherms (bottom) of two-dimensional natural convection at $Ra = 10^6$, $10^7$ and $10^8$.

## 4. Results and discussion

### *4.1. Bifurcation map*

Fig. 3 shows the bifurcation map for different Rayleigh number and the length of fins. There are three different types of flow patterns (steady symmetry, unsteady symmetry and unsteady asymmetry) can be observed in the figure. At relatively low Rayleigh number ($10^6$), the fluid inside the enclosure keeps the flow regime of steady symmetry and dose not vary with the increase of $h$. As for relatively high Rayleigh numbers ($10^8$-$10^9$), the unsteady asymmetry can be always observed regardless of the fin length. When the Rayleigh number increases from $2.5\times10^6$ to $1.0\times10^7$, the transitions of three different flow regimes occur for different $Ra$ and $h$. For a certain $h$, as increasing the Rayleigh number from $10^6$ to $10^9$, the fluid flow changes from steady and symmetry to unsteady and symmetry firstly, and then changes to unsteady asymmetry flow regime. We focus on the nanofluid flow and heat transfer characteristics in these flow pattern. Therefore, the streamlines, temperature distribution and Nusselt number are illustrated in the following sections.

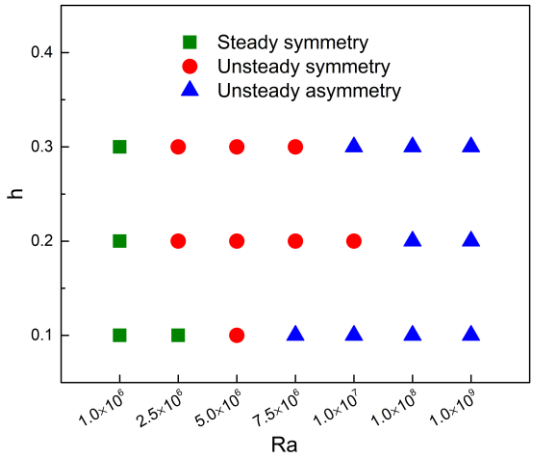


Fig. 3 Bifurcation map for different Rayleigh numbers and $h$ at $\phi = 0.01$.

*4.2. Steady symmetry*

Fig. 4 shows the comparison of streamlines and isotherms between the pure water and nanofluid in the steady symmetry flow regime. As seen in Fig. 4(a), at $Ra = 2.5\times10^6$ and $h = 0.1$, two vortices can be found inside the enclosure which are in clockwise and anticlockwise directions, respectively. The magnitude of fluid flow increases by adding the nanoparticles into the pure water which strengthens the transport energy of the fluid. As a result, the absolute value of maximum of stream function increases with increasing the solid volume fraction. Moreover, it can be observed in Fig. 4(b) that the isothermal lines adjacent to the heating obstacle and four fins cover the shape of them. One thermal plume can be clearly observed above the heat source. The addition of nanoparticles into the base fluid leads to the thickness of thermal boundary layer increases, which causes the decrease of temperature gradient.

**(a)** **(b)**

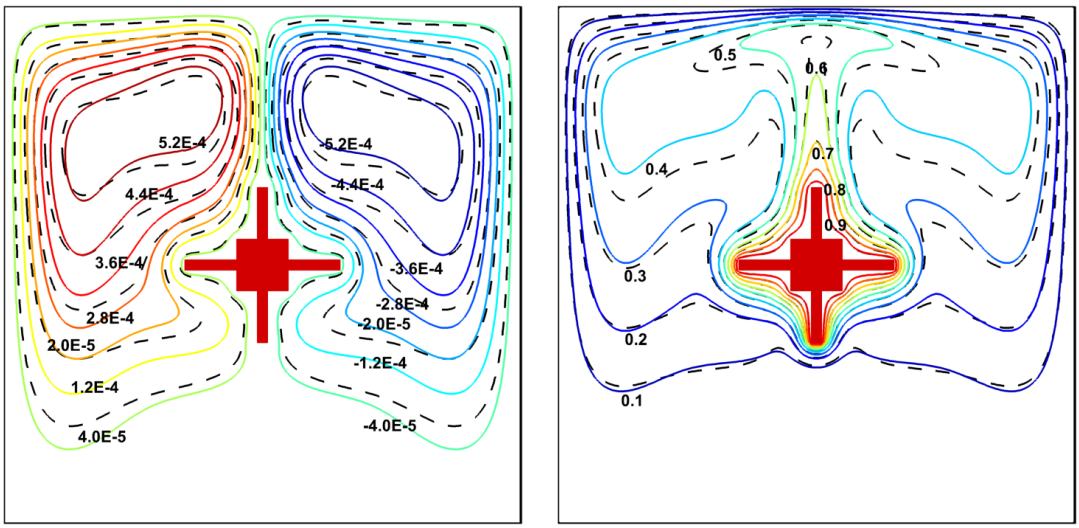


$|\Psi_{\max}|_f = 0.00048$, $|\Psi_{\max}|_{nf} = 0.00071$

Fig. 4 Comparison of streamlines and isotherms at $Ra = 2.5\times10^6$ and $h = 0.1$ between the pure water (dashed lines) and nanofluid (solid lines).

The Streamlines in the steady symmetry flow pattern at $\phi = 0.01$ for different Rayleigh number and length of fins. In this pattern, the flow is steady and the streamlines are symmetrical about the central line. The fluid around the hot source is heated and goes up due to the buoyancy force. For $Ra = 10^6$, at $h = 0.1$, two recirculation cells form on the left and right sides inside the enclosure, respectively. The clockwise vortex is on the right of the anticlockwise vortex. When the length of fins increases to 0.2, the streamlines are squeezed by the longer fins, and this effect is more significant in the horizontal direction. Still, the pattern of streamlines inside the enclosure does not change as increasing the $h$ from 0.1 to 0.2. However, when the $h$ increases to 0.3, the pattern of streamlines changes significantly. Two primary vortices can be observed inside the cavity and each vortex occupies half of the zone. Two secondary vortices are established in one primary vortex due to the small gap between the horizontal fin and the side wall. The directions of two secondary vortices are same to their primary vortex, respectively. Hence the existence of fins impedes and controls fluid flow motion. When the Rayleigh number increases to $2.5\times10^6$ and at $h = 0.1$, the flow pattern is also steady symmetry. Comparing with the pattern of streamlines at $Ra = 10^6$ and $h = 0.1$, it changes distinctly. The two primary vortices at $Ra = 2.5\times10^6$ and $h = 0.1$ are similar to that at

$Ra = 10^6$ and $h = 0.1$. However, two small secondary vortices form inside each primary vortex at $Ra = 2.5\times10^6$ and $h = 0.1$. This is because the increase of Rayleigh number leads to the enhancement of natural convection.

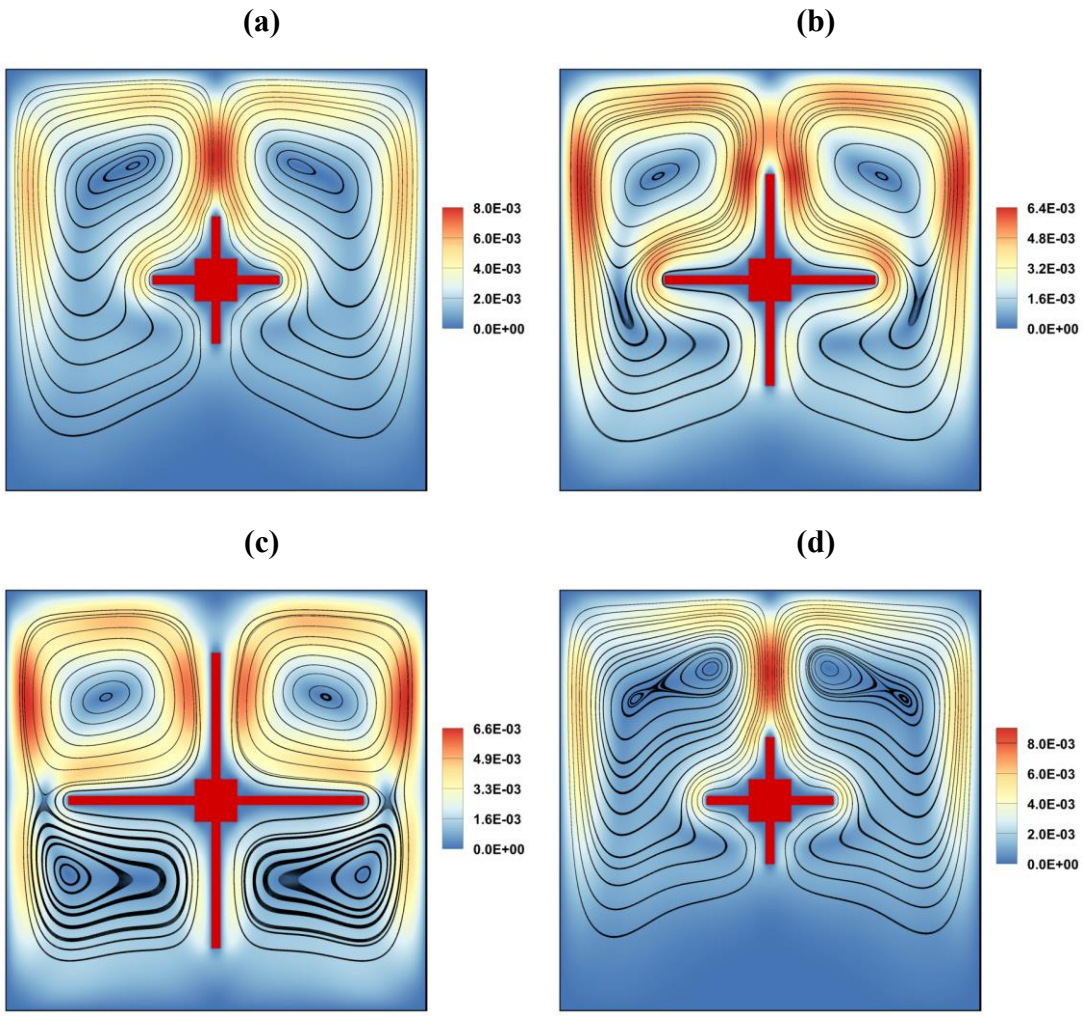


Fig. 5 Streamlines at $\phi = 0.01$ for **(a)** $Ra = 10^6$, $h = 0.1$; **(b)** $Ra = 10^6$, $h = 0.2$; **(c)** $Ra = 10^6$, $h = 0.3$; **(d)** $Ra = 2.5\times10^6$, $h = 0.1$.

Fig. 6 despites the temperature distribution of nanofluid inside the enclosure at different Rayleigh number and $h$. The isothermal lines below the hot source is packed more closely to the hot source than those above the hot source. As seen in Fig. 6(a)-(c), the temperature of each node inside the enclosure increases by increasing the length of fins. This is due to the fact that the increase of $h$ leads to the expansion of heating obstacle surface area. As a result, the cold fluid inside the cavity can be heated much

more easily.

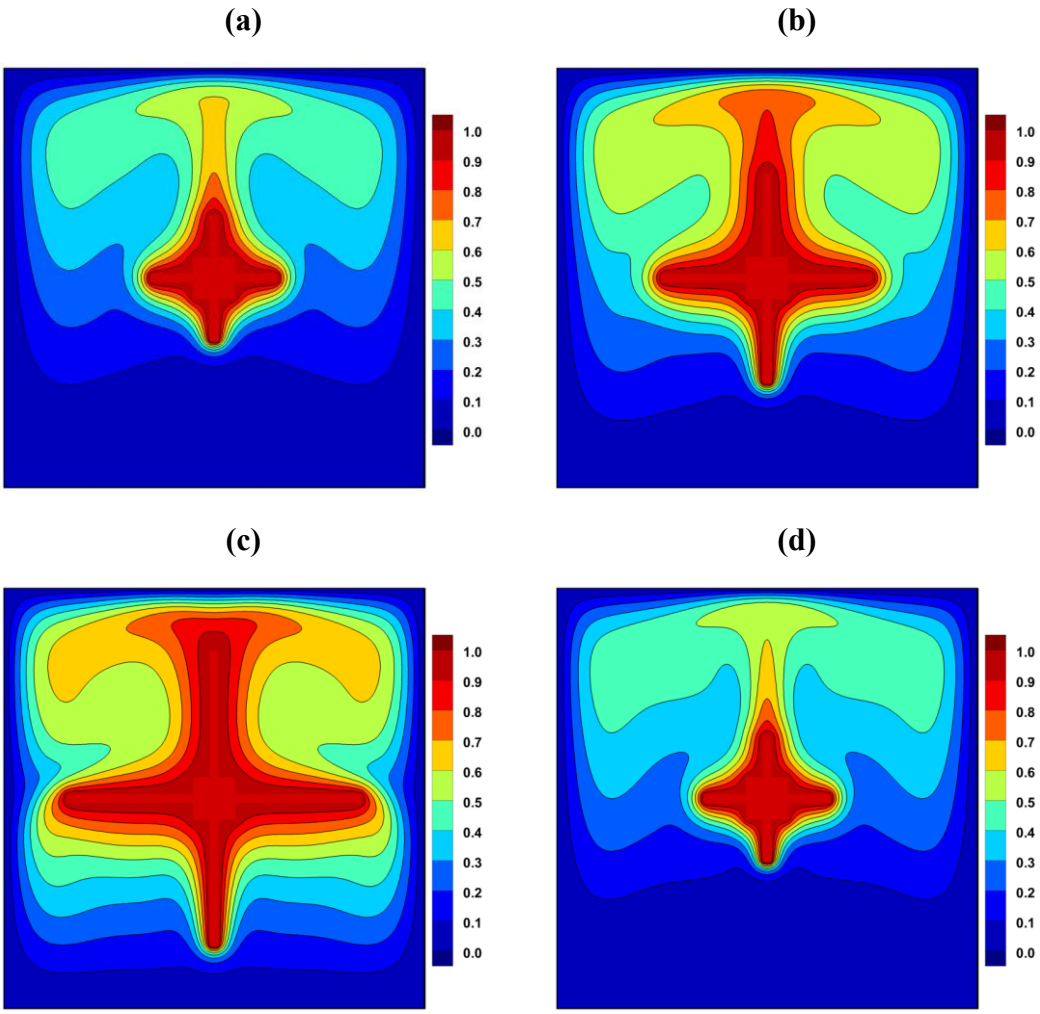


Fig. 6 Isothermal lines at $\phi = 0.01$ for **(a)** $Ra = 10^6$, $h = 0.1$; **(b)** $Ra = 10^6$, $h = 0.2$; **(c)** $Ra = 10^6$, $h = 0.3$; **(d)** $Ra = 2.5\times10^6$, $h = 0.1$.

*4.3. Unsteady symmetry*

As seen in Fig. 3, when the Rayleigh number is larger than $2.5\times10^6$, the flow pattern of unsteady symmetry can be observed. For $\phi = 0.01$, it can be found that the flow pattern is unsteady symmetry at $Ra = 5\times10^6$ for any fin length. Fig. 7 shows the average Nusselt number versus LB time at $Ra = 5\times10^6$ and $\phi = 0.01$ for different $h$. It can be found clearly that the three curves about average Nusselt number have the characteristic of periodicity. At $h = 0.1$ or 0.3, the curves are sinusoidal shape. Moreover, as $h$ increases from 0.1 to 0.3, the mean value of average Nusselt number decreases.

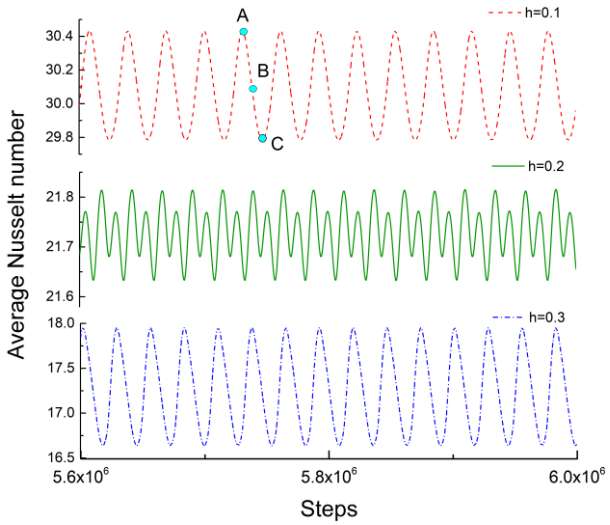


Fig. 7 Average Nusselt number versus steps at $Ra = 5\times10^6$ and $\phi = 0.01$ for different $h$.

In order to illustrate the evolution of the flow and temperature fields in the unsteady symmetry flow regime, the instantaneous streamlines and isotherms in one period are reported. Fig. 8 shows the instantaneous streamlines and isotherms at three moments ($t$ = A, B and C, see Fig. 7) for $Ra = 5\times10^6$, $h = 0.1$ and $\phi = 0.01$. It can be observed from the streamlines that at $t$ = A, only two primary vortices form inside the enclosure and the average Nusselt number achieves the maximum value. When the time is $t$ = B, the vortex inside the primary vortex breaks into two secondary vortices and the upper cell is larger than the lower one. As for $t$ = C, the two secondary vortices vary and the upper cell become lower than the lower one. Also, at this moment, the average Nusselt number reaches the minimum value.

**(a)**

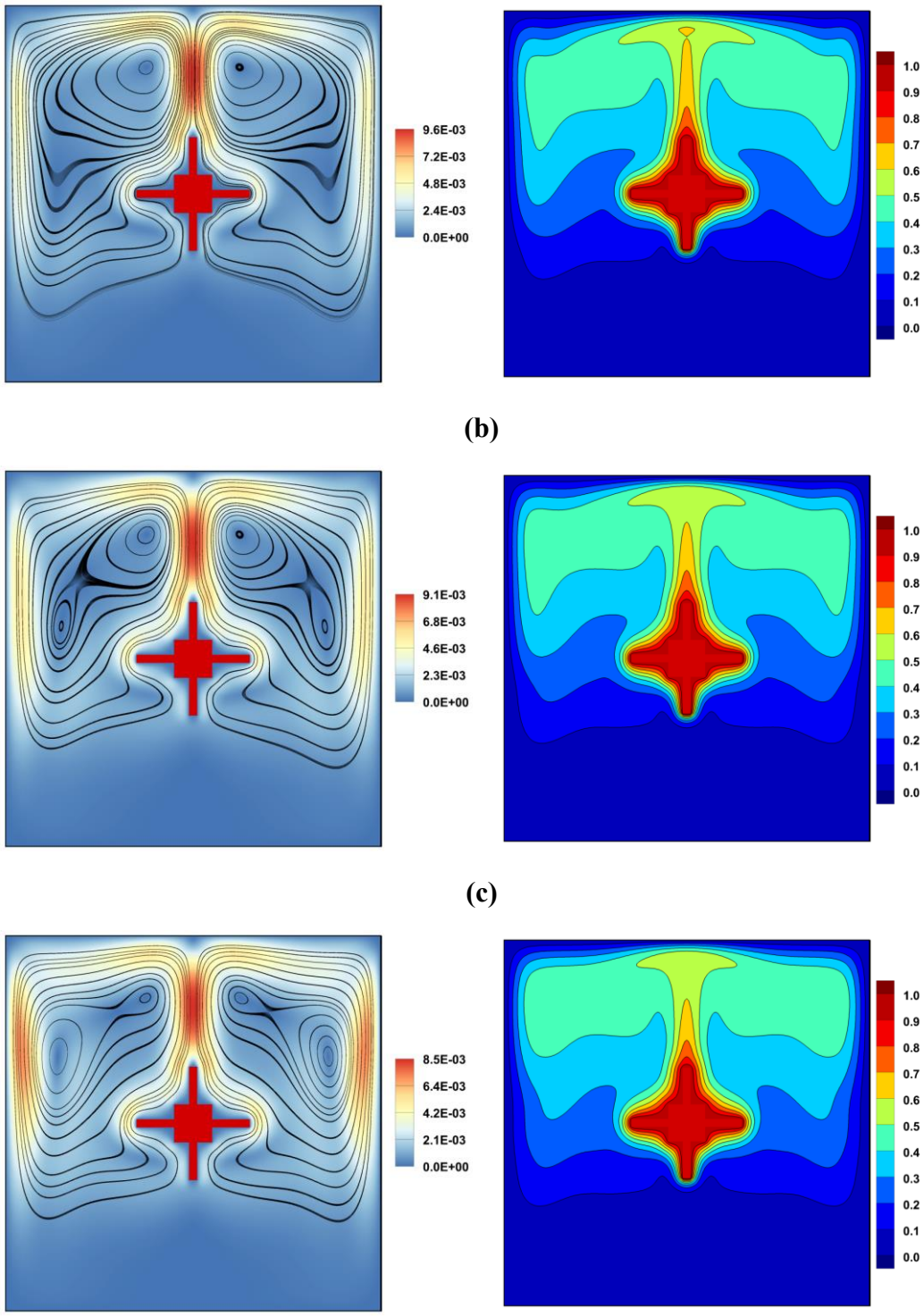


Fig. 8 Streamlines and isotherms at $Ra = 5\times10^6$, $h = 0.1$ and $\phi = 0.01$ at **(a)** $t$ = A; **(b)** $t$ = B; **(c)** $t$ = C.

Fig. 9 presents the fast Fourier transform of average Nusselt number at $Ra = 5\times10^6$ and $\phi = 0.01$ for different $h$ (see Fig. 7), which expresses the power spectrum. It can be found that there is one frequency for $h = 0.1$ and 0.3. However, at $h = 0.2$, two different

frequencies can be observed.

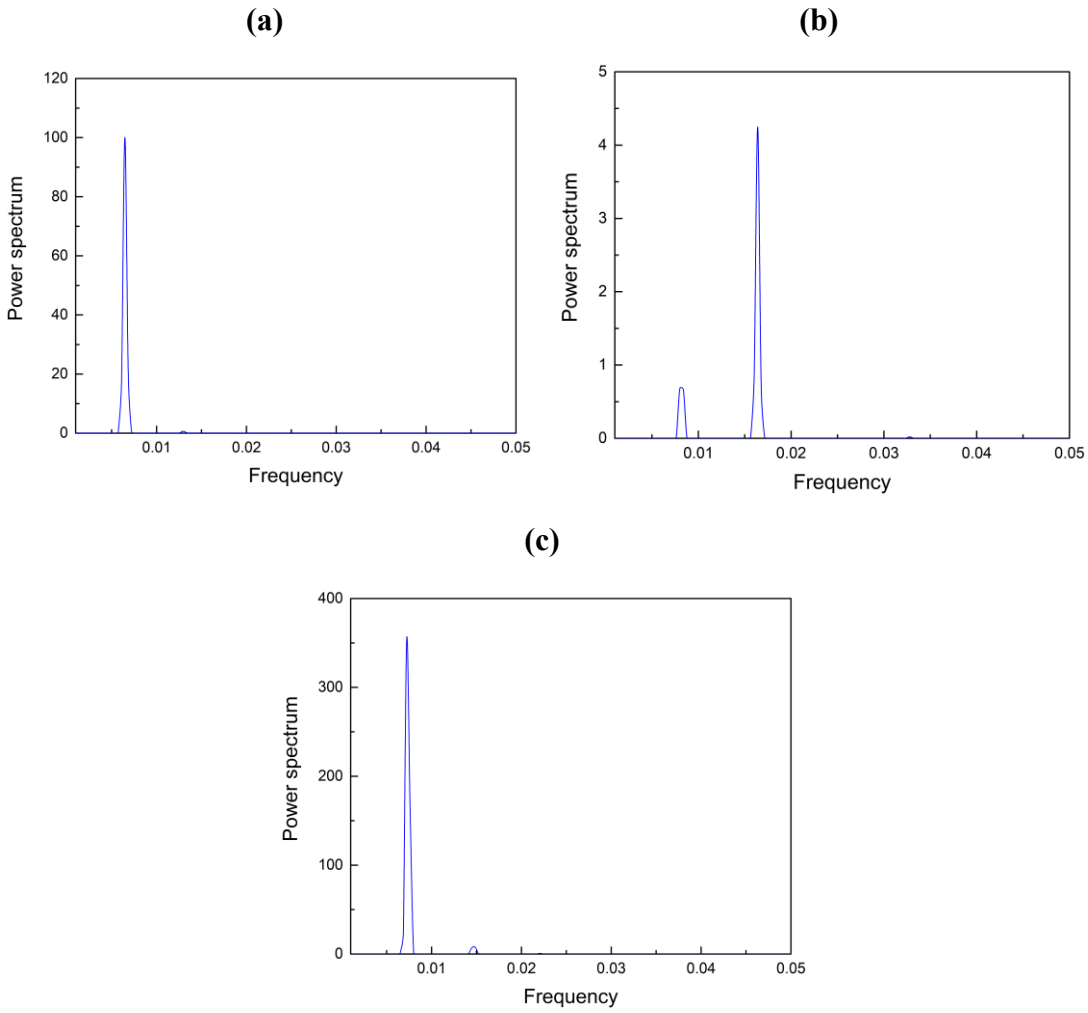


Fig. 9 Fast Fourier transform of $Nu$ signals $Ra = 5\times10^6$ and $\phi = 0.01$ for **(a)** $h = 0.1$; **(b)** $h = 0.2$ **(c)** $h = 0.3$.

To verify the existence of the periodicity in the present flow pattern, the phase diagrams of two monitoring points ($P_1$ and $P_2$, see Fig. 1) are shown in Fig. 10 and Fig. 11. In these phase diagrams, the signal of velocity in the horizontal and vertical directions ($U$ and $V$) are plotted along the horizontal and vertical axis ($X$ and $Y$), respectively. After long time, the curves in the phase diagrams become enclosed shapes, which illustrates the periodic behavior of the fluid in the flow pattern of unsteady symmetry.

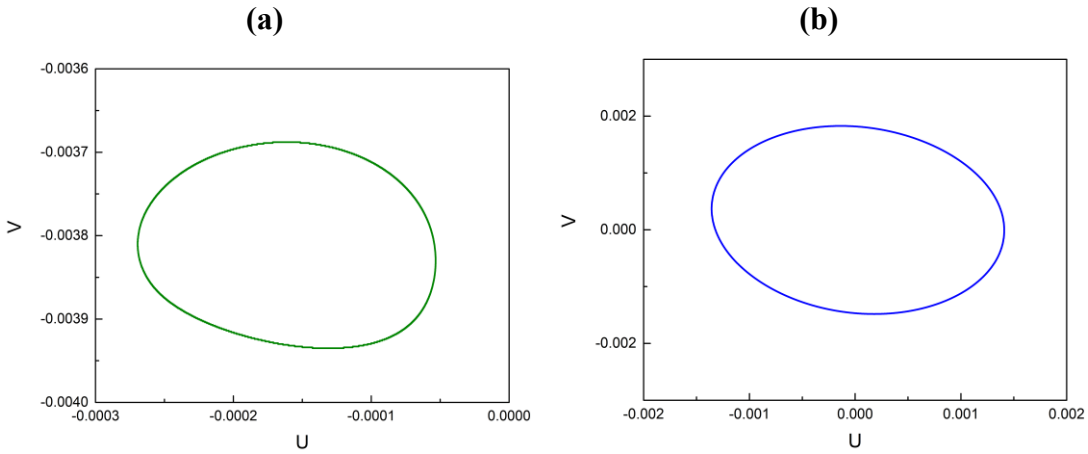


Fig. 10 Phase diagrams at $Ra = 2.5\times10^6$, $h = 0.2$ and $\phi = 0.01$ on **(a)** $P_1$; **(b)** $P_2$.

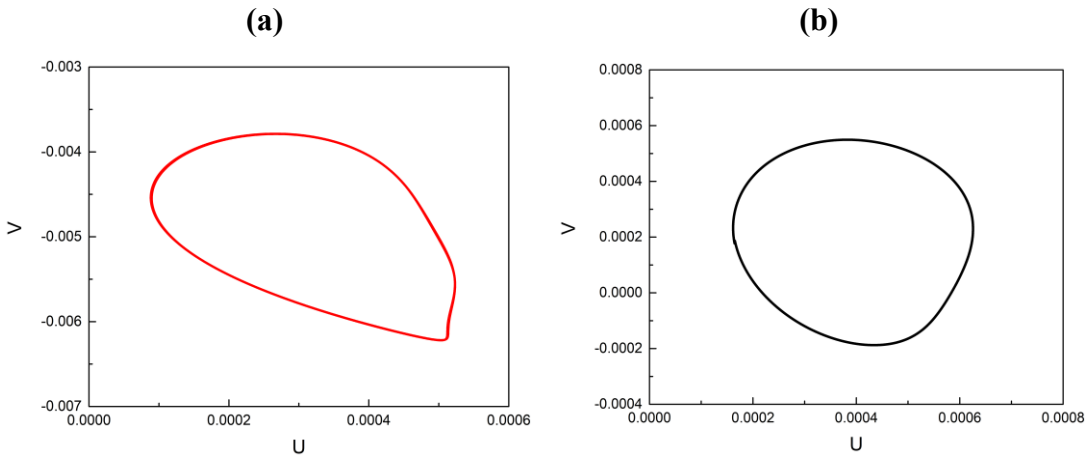


Fig. 11 Phase diagrams at $Ra = 5\times10^6$, $h = 0.3$ and $\phi = 0.01$ on **(a)** $P_1$; **(b)** $P_2$.

Fig. 12 shows the effect of nanoparticle volume fraction on the average Nusselt number at $Ra = 5\times10^6$ and $h = 0.1$. The variation of mean value of average Nusselt number indicates that the average $Nu$ increases by increasing the solid volume fraction. Moreover, the amplitude of average $Nu$ is a decrease function of the nanoparticle volume fraction. Especially at $\phi = 0.05$, the average $Nu$ becomes a constant value and the flow pattern accordingly becomes steady symmetry.

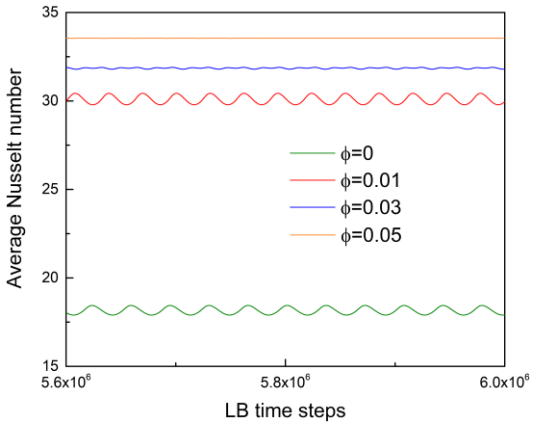


Fig. 12 Effect of nanoparticle volume fraction on the average Nusselt number at $Ra$ = $5\times10^6$ and $h$ = 0.1.

*4.4. Unsteady asymmetry*

When the Rayleigh number is large enough for certain h and $\phi$, the flow pattern evolves into the unsteady asymmetry mode. Fig. 13 shows the instantaneous velocity contour, streamlines and isothermal lines at $Ra$ = $1\times10^9$, $\phi$ = 0.01 and $h$ = 0.2, which is the unsteady asymmetry flow pattern. Both the streamlines and isotherms are very complicated, disordered, asymmetrical and hard to anticipate. Due to the high Rayleigh number, the convection heat transfer is enhanced and a number of recirculation cells can be discovered inside the enclosure.

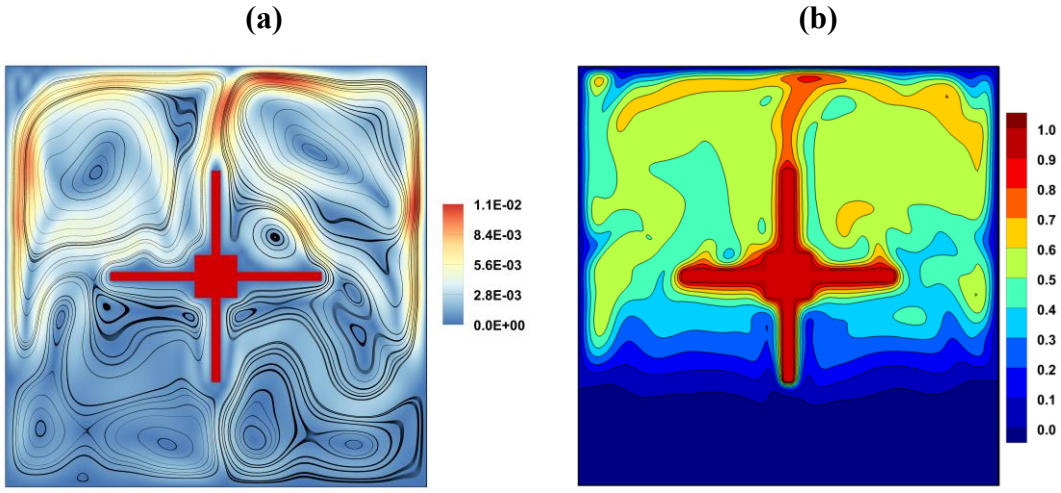


Fig. 13 Instantaneous velocity contour, streamlines and isotherms at $Ra$ = $1\times10^9$, $\phi$ = 0.01 and $h$ = 0.2.

The phase diagram on the point of $P_1$ at $Ra = 10^9$, $h = 0.2$ and $\phi = 0.01$ is depicted in Fig. 14. It's not hard to find that the curve is disorganized and the characteristics of periodicity occurs in the phase diagram, which illustrates the aperiodic unsteady feature of the flow pattern.

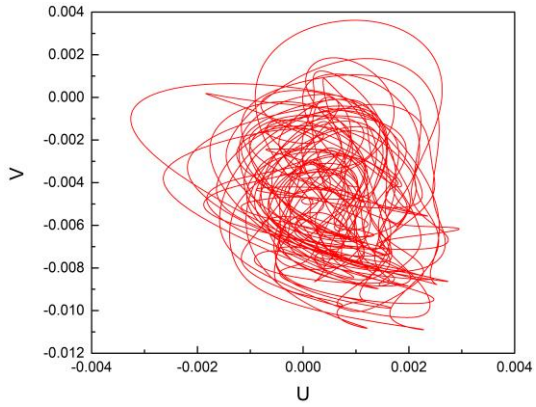


Fig. 14 Phase diagram on $P_1$ at $Ra = 10^9$, $h = 0.2$ and $\phi = 0.01$.

## 5. Conclusion

In the present paper, a new method (SHSLBM) developed from lattice Boltzmann method was used to simulate hybrid nanofluid flow and heat transfer in a thermal energy storage with four fins at high Rayleigh numbers ($10^6 \leq Ra \leq 10^9$). The effects of Rayleigh number, nanoparticle volume fraction and length of fin on the flow pattern, temperature distribution and heat transfer characteristics were reported. The following remarks can be obtained:

- SHSLBM is an especially promising approach for solving the problems of turbulent flow and heat transfer.
- Three kinds of flow patterns (steady symmetry, unsteady symmetry and unsteady asymmetry) can be observed at various Rayleigh number.
- When the *Ra* increases from $1\times10^6$ to $1\times10^9$, the transitions of flow regime from steady symmetry state to unsteady asymmetry state occur, through the unsteady symmetry flow pattern. The steady symmetry flow pattern cannot change to unsteady asymmetry directly by increasing *Ra*.

- The $\phi$ affects the flow pattern significantly. For instance, at $Ra = 5\times10^6$ and $h = 0.1$, the flow inside the enclosure is steadier at higher $\phi$.
- The length of fins also affects the flow pattern. The effect of $h$ on the flow pattern varies at different $Ra$. In the same flow pattern, i.e. at $Ra = 5\times10^6$ and $\phi = 0.01$, there is one frequency for $h = 0.1$ and 0.3, but two different frequencies at $h = 0.2$.
- For different h and $\phi$, the critical Rayleigh number where the flow pattern changes from steady symmetry to unsteady asymmetry is different.

## References


[1] Das D, Roy M, Basak T. Studies on natural convection within enclosures of various (non-square) shapes–A review. International Journal of Heat and Mass Transfer. 2017 Mar 1;106:356-406.

[2] Dawood HK, Mohammed HA, Sidik NA, Munisamy KM, Wahid MA. Forced, natural and mixed-convection heat transfer and fluid flow in annulus: A review. International Communications in Heat and Mass Transfer. 2015 Mar 1;62:45-57.

[3] Öztop HF, Estellé P, Yan WM, Al-Salem K, Orfi J, Mahian O. A brief review of natural convection in enclosures under localized heating with and without nanofluids. International Communications in Heat and Mass Transfer. 2015 Jan 1;60:37-44.

[4] Amber I, O'Donovan TS. Natural convection induced by the absorption of solar radiation: A review. Renewable and Sustainable Energy Reviews. 2018 Feb 1;82:3526-45.

[5] Bhardwaj S, Dalal A, Pati S. Influence of wavy wall and non-uniform heating on natural convection heat transfer and entropy generation inside porous complex enclosure. Energy. 2015 Jan 1;79:467-81.

[6] Esfe MH, Arani AA, Yan WM, Ehteram H, Aghaie A, Afrand M. Natural convection in a trapezoidal enclosure filled with carbon nanotube–EG–water nanofluid. International Journal of Heat and Mass Transfer. 2016 Jan 1;92:76-82.

[7] Ma Y, Mohebbi R, Rashidi MM, Yang Z, Sheremet MA. Numerical study of MHD nanofluid natural convection in a baffled U-shaped enclosure. International Journal of Heat and Mass Transfer. 2019 Mar 1;130:123-34.

[8] Haghighi SS, Goshayeshi HR, Safaei MR. Natural convection heat transfer enhancement in new designs of plate-fin based heat sinks. International Journal of Heat and Mass Transfer. 2018 Oct 31;125:640-7.

[9] Ma Y, Mohebbi R, Rashidi MM, Yang Z. Study of nanofluid forced convection heat transfer in a bent channel by means of lattice Boltzmann method. Physics of Fluids. 2018 Mar;30(3):032001.

[10] Ma Y, Mohebbi R, Rashidi MM, Yang Z. Effect of hot obstacle position on natural convection heat transfer of MWCNTs-water nanofluid in U-shaped enclosure using lattice Boltzmann method. International Journal of Numerical Methods for Heat & Fluid Flow. 2019 Jan 7;29(1):223-50.

[11] Ma Y, Mohebbi R, Rashidi MM, Yang Z. MHD convective heat transfer of Ag-MgO/water hybrid nanofluid in a channel with active heaters and coolers. International Journal of Heat and Mass Transfer. 2019 Jul 1;137:714-26.

[12] Hatami M, Safari H. Effect of inside heated cylinder on the natural convection heat transfer of nanofluids in a wavy-wall enclosure. International Journal of Heat and Mass Transfer. 2016 Dec 1;103:1053-7.

[13] Chikatamarla SS, Karlin IV. Entropic lattice Boltzmann method for multiphase flows. Physical review letters. 2015 May 1;114(17):174502.

[14] Chen Z, Shu C, Tan D. High-order simplified thermal lattice Boltzmann method for incompressible thermal flows. International Journal of Heat and Mass Transfer. 2018 Dec 1;127:1-6.

[15] Jami M, Moufekkir FA, Mezrhab A, Fontaine JP, Bouzidi MH. New thermal MRT lattice Boltzmann

method for simulations of convective flows. International Journal of Thermal Sciences. 2016 Feb 1;100:98-107.

[16] Chen Z, Shu C, Tan D, Wu C. On improvements of simplified and highly stable lattice Boltzmann method: Formulations, boundary treatment, and stability analysis. International Journal for Numerical Methods in Fluids. 2018 Jun 10;87(4):161-79.

[17] Mohamad A A, Kuzmin A. A critical evaluation of force term in lattice Boltzmann method, natural convection problem[J]. International Journal of Heat and Mass Transfer, 2010, 53(5-6): 990-996.

[18] de Vahl Davis G. Natural convection of air in a square cavity: a bench mark numerical solution. International Journal for numerical methods in fluids. 1983 May;3(3):249-64.

[19] Chen Z, Shu C, Tan D. A simplified thermal lattice Boltzmann method without evolution of distribution functions. International Journal of Heat and Mass Transfer. 2017 Feb 1;105:741-57.